Bioactive Materials 10 (2022) 295–305

Contents lists available at ScienceDirect

Bioactive Materials

journal homepage: www.sciencedirect.com/journal/bioactive-materials

2D antimonene-integrated composite nanomedicine for augmented low-temperature photonic tumor hyperthermia by reversing cell thermoresistance

Jianrong Wu [a,1], Xiaojun Cai [a,1], Gareth R. Williams [b], Zheying Meng [a], Weijuan Zou [a], Li Yao [a], Bing Hu [a,**], Yu Chen [c,***], Yuanyi Zheng [a,d,*]

[a] Department of Ultrasound in Medicine, Shanghai Jiao Tong University Affiliated Sixth People's Hospital, Shanghai, 200233, PR China
[b] UCL School of Pharmacy, University College London, London, WC1N 1AX, UK
[c] Materdicine Lab, School of Life Sciences, Shanghai University, Shanghai, 200050, PR China
[d] State Key Laboratory of Oncogenes and Related Genes, School of Medicine, Shanghai Jiao Tong University, Shanghai, 200233, PR China

ARTICLE INFO

Keywords:
Antimonene
Heat shock proteins
Photothermal therapy
Glucose oxidase
Calcium carbonate

ABSTRACT

The overexpression of heat shock proteins (HSPs) in tumor cells can activate inherent defense mechanisms during hyperthermia-based treatments, inducing thermoresistance and thus diminishing the treatment efficacy. Here, we report a distinct "non-inhibitor involvement" strategy to address this issue through engineering a calcium-based nanocatalyst (G/A@$CaCO_3$-PEG). The constructed nanocatalyst consists of calcium carbonate ($CaCO_3$)-supported glucose oxidase (GOD) and 2D antimonene quantum dots (AQDs), with further surface modification by lipid bilayers and polyethylene glycol (PEG). The engineered G/A@$CaCO_3$-PEG nanocatalyst features prolonged blood circulation, which is stable at neutral pH but rapidly degrades under mildly acidic tumor microenvironment, resulting in rapid release of drug cargo in the tumor microenvironment. The integrated GOD effectively catalyzes the depletion of glucose for reducing the supplies of adenosine triphosphate (ATP) and subsequent down-regulation of HSP expression. This effect then augments the therapeutic efficacy of photothermal hyperthermia induced by 2D AQDs upon irradiation with near-infrared light as assisted by reversing the cancer cells' thermoresistance. Consequently, synergistic antineoplastic effects can be achieved via low-temperature photothermal therapy. Systematic *in vitro* and *in vivo* evaluations have demonstrated that G/A@$CaCO_3$-PEG nanocatalysts feature potent antitumor activity with a high tumor-inhibition rate (83.92%). This work thus paves an effective way for augmenting the hyperthermia-based tumor treatments via restriction of the ATP supply.

1. Introduction

Numerous emerging anticancer treatments are currently in clinical trials [1,2], with the aim to achieve more effective and targeted treatments than conventional chemo- or radiotherapy can deliver. In particular, hyperthermia-based treatments, principally nanomedicine-involved photothermal therapy (PTT) and magnetic hyperthermia, have received ever-increasing attention owing to their physical targeting feature, noninvasiveness and high therapeutic efficacy [3–6]. Photothermally-active nanoparticles (NPs) can induce hyperthermia under light irradiation, enabling them to ablate tumors by photonic irradiation, which have been extensive explored in cancer treatment [7,8]. Also, combination strategies with PTT provide a promising treatment method to overcome some impediments of single PTT, which has increasingly attracted extensive attention [9]. The generated heat during PTT also improves the intracellular delivery and release of drugs, immunologic adjuvant, genes, and photosensitizer, which allows PTT to combine with other treatments for enhanced

Peer review under responsibility of KeAi Communications Co., Ltd.
* Corresponding author. Department of Ultrasound in Medicine, Shanghai Jiao Tong University Affiliated Sixth People's Hospital, Shanghai, 200233, PR China.
** Corresponding author.
*** Corresponding author.
E-mail addresses: hub@sjtu.edu.cn (B. Hu), chenyuedu@shu.edu.cn (Y. Chen), zhengyuanyi@sjtu.edu.cn (Y. Zheng).
[1] These authors contribute equally to this work.

https://doi.org/10.1016/j.bioactmat.2021.08.018
Received 10 June 2021; Received in revised form 2 August 2021; Accepted 15 August 2021
Available online 19 August 2021

efficacy. However, there exists some undesirable limitations hindering the clinical translation of PTT. For instance, the induction of high local temperatures at the tumor site and nonspecific heat diffusion can result in damage to surrounding healthy tissues [10]. Also, the inadequate generation of heat deeply inside the tumor may cause the recurrence of cancer and metastasis [11,12]. The intrinsic thermoresistance of cancer cells is inescapably problematic [13,14]. Heat shock proteins (HSPs), including HSP90 and HSP70, play a key role in initiating the defense mechanism of tumor in thermoresistance [15,16].

To solve these critical issues, several strategies have been proposed to reverse the resistance of cancer cells to thermal stresses. HSP inhibitors (e.g., gambogic acid [17], siRNA [18], 17-allylamino-17-demethoxygeldanamycin [19,20]) have been extensively employed to circumvent the issue of thermoresistance, resulting in effective low-temperature PTT. A combination of HSP inhibitors and photothermal agents is thus expected to enhance the PTT efficiency. However, these cookie-cutter approaches generally require high dose of HSP inhibitors, which have some significant limitations, such as high dose, undesirable toxic side effects, uncontrollable inhibitor release, etc. These issues thus hinder the further clinical translation of PTT. Intrinsically, HSP expression depends on energy supply of adenosine triphosphate (ATP), which is critically important to guarantee protein synthesis and cell growth [21,22]. Based on this aspect, restricting ATP supply can indirectly inhibit the hyperthermia-induced upregulation of HSPs, thereby reversing the HSP-dependent tumor thermoresistance. This strategy also enables efficient low-temperature PTT without inhibitors involvement. Therefore, coupling photothermal-conversion agents with ATP-regulation nanosystem that can disrupt energy sources has been regarded as a distinct and effective strategy to deal with the tumor thermoresistance in PTT.

Two-dimensional (2D) nanomaterials have recently been substaintially explored for diverse biomedical applications, including gene/drug delivery, photonic nanotherapy, bioimaging, and biosensing [23–26]. As a typical emerging material, black phosphorus recently attracted scientific interest for comprehensive applications, especially in biomedical fields [27]. A great deal of phosphorus-based nanomaterials has been conducted and widespread use [28,29]. Given the similarities of morphological characteristics between black phosphorus and other 2D materials of group VA (e.g. arsenene, antimonene, and bismuthene), these 2D materials are expected to exhibit are expected to show great potential in a variety of applications [30]. Of these, one emergent nanosystem is 2D antimonene, which comprises sheets of sp^3-hybridised Sb atoms with a structure analogous to graphene [31]. Antimonene can be generally prepared through liquid exfoliation from bulk antimony, which features the distinct thermoelectric property, chemical stability, optical absorption and superconductivity [32]. Meanwhile, the honeycomb structure of antimonene makes it suitable for drug/gene/immunosuppressor loading and delivery, indicates its promising potentials for applications in cancer chemo/gene-photothermal or photothermal/immune combination therapy [23,33]. Particularly, Sb-based nanomaterials exhibit the near-infrared (NIR) absorption, endowing them with desirable photothermal property and contrast-enhanced photoacoustic (PA) imaging capability [34,35]. For example, the previously reported antimonene nanosheet and quantum dots (AQDs) possessed superior thermal conductivity and high photothermal conversion efficacy of 41.8% and 45.5%, respectively [23,34]. In addition, the Sb nanocrystal even demonstrated good photothermal property in the near-infrared-II window [36]. Hence, we expected that 2D antimonene may induce excellent photothermal effects similar to those of emerging 2D nanomaterials. However, their potential for application in reversing the thermoresistance of the cancer cells and realizing low-temperature PTT remains unexplored.

Calcium carbonate ($CaCO_3$) NPs have been explored extensively in biomedicine due to the intrinsic biocompatibility, pH-sensitivity, and biodegradability [37,38]. In this work, the rational integration of calcium-based biomineral and single-element 2D nanomaterials was conducted to engineer a "non-inhibitor involvement" nanosystem for photonic hyperthermia-based tumor nanotherapy. $CaCO_3$ NPs were employed as a nanocarrier matrix to fabricate a pH-sensitive nanocatalyst (G/A@$CaCO_3$-PEG) comprising $CaCO_3$ loaded with AQDs and glucose oxidase (GOD), with additional surface PEGylation. This formulation was further explored for enhanced low-temperature PTT (Scheme 1). $CaCO_3$ NPs synthesized via a gas diffusion method were utilized as a template to direct the formulation of G/A@$CaCO_3$ by co-precipitation. The engineered G/A@$CaCO_3$ nanocatalyst is expected to be rapidly degraded under the mildly acidic pH within the tumor microenvironment, leading to the release of the loaded GOD and AQDs components. The integrated AQDs effectively converted NIR laser to localized heat upon irradiation, allowing for PTT. Simultaneously, the released GOD catalyzes the oxidation of glucose. This glucose-depletion process is capable of restricting ATP supply and consequently leading to HSP down-regulation [39], which attenuates the thermoresistance of the tumor cells. In addition, based on the strong NIR absorption of 2D AQDs, the G/A@$CaCO_3$ system acts as the contrast agents for PA imaging. The enhanced, synergistic and PA imaging-guided photonic hyperthermia was systematically demonstrated both *in vitro* at cellular level and *in vivo* on SW1990 tumor-bearing mice.

2. Materials and methods

2.1. Materials

Pulverized antimony (Sb) powder, calcium chloride ($CaCl_2{\cdot}2H_2O$), 1,2-dioleoyl-*sn*-glycero-3-phosphate (sodium salt; DOPA), ammonium bicarbonate (NH_4HCO_3), and 1,2-dipalmitoyl-snglycero-3-phosphocholine (DPPC) were purchased from the Aladdin Reagent Co. (Shanghai, China). Cholesterol was purchased from J&K Scientific Ltd (Shanghai, China). 1,2-distearoyl-*sn*-glycero-3-phosphoethanolamine-*N*-[methoxy (poly ethylene glycol)] (DSPE-PEG_{5000}) was acquired from Yanyi Biotech, Inc. (Shanghai, China). GOD, calcein acetoxymethyl ester-AM (Calcein-AM) and propidium iodide (PI) were purchased from Sigma-Aldrich Trading Co., Ltd. (Shanghai, China). Cell Counting Kit-8 (CCK-8), ATP, BCA protein and Annexin V/PI cell assay kits were purchased from Dojindo Laboratories (Kumamoto, Japan). Bradford protein assay kits were bought from Beyotime Biotechnology (Shanghai, China). RIPA lysate was ordered from Beyotime (Shanghai, China). Dulbecco's modified eagle medium (DMEM), Roswell park memorial institute (RPMI-1640) medium, fetal bovine serum (FBS), and penicillin/streptomycin were supplied by Thermo Scientific (Beijing, China). Deionized (DI) water (18.2 MΩ cm) was used in all experiments. All the other chemicals and reagents were of analytical grade and used as received.

2.2. Characterization

Transmission electron microscopy (TEM) images and corresponding elemental mapping images were measured for the morphology and elemental composition of the NPs using a JEM-2100F field emission TEM (JEOL, Tokyo, Japan). X-ray diffraction (XRD, D8 ADVANCE, Bruker, Germany) and X-ray photoelectron spectroscopy (XPS, ESCALAB 250Xi, ThermoFisher, Waltham, MA, USA) were used to determine the physical form and chemical composition of AQDs. Raman spectra were measured using a Horiba Jobin Yvon Labram HR-800 Raman spectrometer (Paris, France). The hydrodynamic particle size was determined on a Malvern Zetasizer Nanoseries (Nano ZS90, Malvern, UK). Ultraviolet–visible–near-infrared (UV–vis–NIR spectra) were recorded by using a UV-1700 PC spectrometer (Shimadzu, Tokyo, Japan). The contents of Ca^{2+} and AQDs were quantified by inductively coupled plasma optical emission spectroscopy (ICP-OES, Prodigy 7, Leeman Laboratories, Hudson, NH, USA).

2.3. Fabrication of PEG-Coated AQDs

AQDs were prepared through a top-down approach by coupling bath

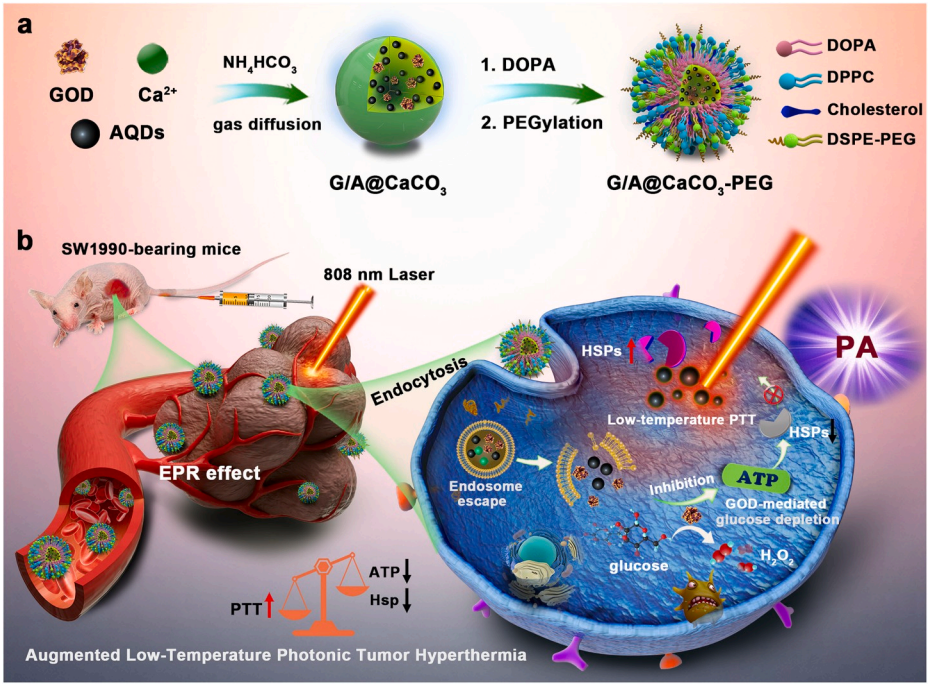

Scheme 1. Schematic illustration of (a) the construction of G/A@$CaCO_3$-PEG nanocatalysts and (b) their detailed therapeutic procedure and mechanism. The formulation is based on $CaCO_3$ NPs, which co-encapsulate AQDs and GOD, followed by surface PEGylation. This system that integrates GOD can catalyze the depletion of glucose for reducing the supplies of ATP and subsequent down-regulation of HSP expression, and in turn the efficiency of low-temperature photonic tumor hyperthermia is augmented.

and probe sonication liquid phase exfoliation [34]. A commercial Sb powder with initial concentration of 20 mg/mL was dispersed in ethanol. The Sb solution was sonicated for 10 h in an ice-bath at 500 W with ultrasound probe, and then for another 5 h at 300 W in an ultrasonic bath. Subsequently, the mixture was further exfoliated via probe sonication at 500 W for 8 h in an ice-bath. The resultant suspension was centrifuged (3000 rpm) for 30 min and the supernatant containing AQDs was collected for future use. For surface PEGylation, AQDs (5 mg) were dispersed in chloroform (50 mL), followed by the addition of DSPE-PEG (50 mg). After probe sonication (100 W) for 20 min and stirring for 2 h, the mixture was filtered and chloroform was removed with a rotary evaporator. The obtained AQDs-PEG NPs were re-dispersed in water, centrifuged at 12000 rpm for 10 min, and washed with deionized water for three times. The final AQDs-PEG products were re-suspended in water and stored at 4 °C for future use.

2.4. Synthesis of G/A@$CaCO_3$-PEG

$CaCO_3$ NPs were synthesized via a gas diffusion method, and then were utilized as a template to direct the formulation of G/A@$CaCO_3$ by co-precipitation [38]. Typically, $CaCl_2{\cdot}2H_2O$ (100 mg) was dissolved in anhydrous ethanol (100 mL) and the AQDs-PEG dispersion (250 μL, 1 mg/mL) was added dropwise with rapid stirring for 1 h. Subsequently, GOD aqueous solution (5 mL, 10 mg/mL) was added. The reaction mixture was transferred into a glass bottle covered by aluminum foil and then placed in a sealed container with dry NH_4HCO_3 (5 g). After keeping the whole system under vacuum at 40 °C for 12 h, the product was collected by centrifugation (8000 rpm) and washed with ethanol for several times. Finally, the G/A@$CaCO_3$ NPs were re-dispersed in ethanol for further use.

To improve physiological stability, the obtained G/A@$CaCO_3$ NPs were coated with DSPE-PEG_{5000} via a two-step method according to the previous work [40]. Briefly, G/A@$CaCO_3$ dispersion (5 mL, 4 mg/mL) and DOPA solution in chloroform (1 mL, 4 mg/mL) were mixed, which was sonicated for 0.5 h in an ultrasonic bath (100 W). The DOPA-modified G/A@$CaCO_3$ was then collected by centrifugation (6000 rpm) and re-dispersed in chloroform, followed by mixing with 4 mL of chloroform solution of DPPC, cholesterol and DSPE-PEG_{5000} at a molar ratio of 5:5:2. After being vigorously stirred overnight, the chloroform was removed by rotary evaporation. The dried solid was dispersed in phosphate buffered saline (PBS) and sonicated for hydration. Finally, the obtained G/A@$CaCO_3$-PEG NPs were purified by repeated centrifugation (13000 rpm) and re-dispersed in ethanol for further use. Meanwhile, bare $CaCO_3$-PEG NPs, GOD loaded $CaCO_3$-PEG (G@$CaCO_3$-PEG), and AQD loaded $CaCO_3$-PEG (A@$CaCO_3$-PEG) were prepared by following the same procedure except that the relevant precursors were not added. The amount of GOD was measured by a Bradford protein assay kits according to the manufacturer's instructions. Meanwhile, the Ca^{2+} and AQDs contents of G/A@$CaCO_3$-PEG were detected by ICP-OES.

2.5. Measurement of photothermal performance of G/A@$CaCO_3$-PEG

G/A@$CaCO_3$-PEG aqueous dispersions (200 μL) at different concentrations (20, 50, 100 and 200 μg/mL) were loaded into an Eppendorf tube and each sample was exposed to an 808 nm NIR laser at different power densities (0.3, 0.5, 0.8, 1.0 W/cm^2) for 5 min. During irradiation, the real-time temperatures of the solutions were recorded using an IR thermal camera (TI100 Infrared Camera FLKTI100 9HZ, FLUKE, Shanghai, China). DI water was used as a negative control. To evaluate the photostability of G/A@$CaCO_3$-PEG NPs under NIR laser irradiation, an aqueous dispersion (100 μg/mL) was exposed to an 808 nm laser at 0.8 W/cm^2 for 5 min then naturally cooled for 5 min. This was repeated over five on-off cycles. The photothermal conversion efficiency of AQDs and G/A@$CaCO_3$-PEG was ascertained using the literature procedure and calculated using the following equation.

$$\eta = \frac{hS(T_{max} - T_{amb}) - Q_0}{I\left(1 - 10^{-A}\right)} \quad (1)$$

S and h represent the surface area and the heat transfer coefficient. T_{max} is the equilibrium temperature and T_{amb} the ambient temperature. Q_0 is the heat absorption of the quartz container, I is the laser power density, and A is the absorbency of the samples at 808 nm.

2.6. In vitro degradation experiments

G/A@$CaCO_3$-PEG was dispersed in PBS at different pH values (pH

5.0, 6.5 and 7.4) under constant shaking at 37 °C. At designated time intervals, 1 mL of medium was withdrawn from each sample and centrifuged for TEM analysis, and the released Ca^{2+} quantified by ICP-OES analysis.

2.7. Catalytic activity of G/A@$CaCO_3$-PEG

A@$CaCO_3$-PEG and G/A@$CaCO_3$-PEG suspensions (100 μg/mL) at different pH values were added into glucose solution (1 mg/mL) with the addition of H_2O_2 (50 μM) at room temperature. At different time intervals, different samples were collected and the concentration of glucose was measured with an Accu-Chek Active glucometer (Roche, Shanghai, China). A pH meter (METTLER TOLEDO, Shanghai, China) was employed to determine the pH value of the samples.

2.8. Measurement of intracellular ATP levels

SW1990 cells were seeded in 6-well plates at a density of 1×10^5 cells per well and incubated for 24 h. After incubation with A@$CaCO_3$-PEG, free GOD or G/A@$CaCO_3$-PEG for 12 h, the cells were then irradiated or not with an 808 nm laser (0.8 W/cm^2) for 5 min, which were washed with PBS, and harvested with trypsin/EDTA. The cells were then collected by centrifugation (12000 g, 5 min), lysed on ice by RIPA buffer (100 μL/well) and the intracellular ATP level was measured in accordance with the manufacturer's instructions.

2.9. In vitro low-temperature PTT

To investigate the *in vitro* toxicity of G/A@$CaCO_3$-PEG combined with NIR laser treatment to SW1990 cells, the original culture medium was replaced with fresh media containing varied concentrations of G/A@$CaCO_3$-PEG and incubated for 24 h at 37 °C in a humidified 5% CO_2 atmosphere. For the NIR laser treatment group, G/A@$CaCO_3$-PEG was incubated with SW1990 cells at a final concentration of 50 μg/mL for 2 h and then subjected to 5 min laser irradiation at different power densities. After further culturing for a total incubation time of 22 h, a standard CCK-8 assay was used to measure cell viabilities relative to control untreated cells.

To explore the therapeutic efficacy of the combination treatment (mild-temperature PTT and glucose depletion), SW1990 cells were seeded into 96-well plates and then treated with PBS (control), A@$CaCO_3$-PEG (glucose depletion therapy), A@$CaCO_3$-PEG + laser (mild-temperature PTT), G/A@$CaCO_3$-PEG (GOD-mediated glucose depletion therapy), and G/A@$CaCO_3$-PEG + laser (combination therapy). After an additional 24 h incubation at 37 °C, the culture medium was removed and the cells were rinsed with PBS three times before relative cells viabilities were evaluated with the CCK-8 assay.

Cell viabilities were additionally evaluated with a live/dead cell staining assay. After subjecting SW1990 cells to the various treatments detailed above, the cells were stained with calcein-AM (10 mM) and PI solutions (10 mM) in PBS for 15 min at 37 °C in the dark. The cells were washed with PBS three times, and subsequently visualized using confocal laser scanning microscopy (CLSM, FV1000, Olympus Company, Japan).

2.10. Animals and tumor model

BALB/c nude mice (4–5 weeks) and healthy female Kunming mice (6–7weeks) were provided by the Shanghai Slac Laboratory Animal Co., Ltd. (Shanghai, China). All animal experiments were conducted under approval of the Institutional Animal Care and Use Committee (IACUC) of Shanghai Jiao Tong University Affiliated Sixth People's Hospital (Animal Welfare Ethics acceptance number No: DWLL2020-0582). The SW1990 xenograft tumor model was established by inoculating 2×10^7 SW1990 cells in 200 μL PBS into the right armpit region of each mouse. The tumor size was measured with a digital vernier caliper every other day and the tumor volume was calculated according to the formula: volume = (width^2) × (length)/2. The tumor-inhibition rate of each treatment was calculated as (1-V/V_0) × 100% (where V_0 is the tumor volume of the control group and V is that of the treatment groups).

2.11. In vitro and in vivo photoacoustic imaging

For *in vitro* PA imaging, each individual hole on a home-made agar plate was filled with G/A@$CaCO_3$-PEG dispersions at various Sb concentrations (0, 0.5, 1.0, 2.0, 5.0, 10 mM) and then imaged with inVision128 PA equipment (iThera Medical Inc., Germany).

For *in vivo* PA imaging, SW1990-tumor bearing mice were anesthetized and injected with 100 μL of G/A@$CaCO_3$-PEG dispersion (Sb: 3.5 mg/kg) via the tail vein when the tumors were allowed grow to a uniform size of around 100 mm^3. PA imaging was performed using a Vevo LAZR-X PA imaging system (Visual-Sonics Co. Ltd, Toronto, Canada) before injection and then at predetermined time points post intravenous injection of the nanoparticles. The signal intensities of tumors were quantified with the Image J software.

2.12. In vivo antitumor therapy

When the tumors reached the size of around 100 mm^3 in volume, the SW1990-tumor bearing mice were divided at random into five groups and given various treatments: 1) saline, 2) saline + laser, 3) G/A@$CaCO_3$-PEG, 4) A@$CaCO_3$-PEG + laser, 5) G/A@$CaCO_3$-PEG + laser. These mice were injected with different formulations (saline, A@$CaCO_3$-PEG or G/A@$CaCO_3$-PEG) via the tail vein on day 0, 4, and 8. The injected doses of Sb and GOD were 3.5 mg/kg and 4.5 mg/kg, respectively. At 12 h post-injection, Groups 2, 4 and 5 were irradiated with an NIR laser (0.8 W/cm^2) for 5 min to trigger mild hyperthermia (43 °C). A thermal camera (FLIR E50, Fluke, Washington, USA) was employed to monitor the temperature and acquire thermal images.

The weight of each mouse was also monitored every two days. On day 15, the mice from all groups were sacrificed and the tumors were excised and weighed. Then, the intratumoral ATP level was detected using an ATP assay kit. Meanwhile, the major organs including the heart, spleen, lung, liver and kidney were also recovered. All the tissue samples were fixed in a 10% formalin solution and embedded in paraffin for hematoxylin and eosin (H&E) staining. Additionally, the tumor samples were further stained with TdT-mediated dUTP nick-end labeling (TUNEL) for histological analysis, according to the manufacturer's instructions.

2.13. In vivo toxicity evaluation

Female Kunming mice (n = 4) were injected with 200 μL of PBS or G/A@$CaCO_3$-PEG (40 mg/kg) through the tail vein. Blood samples were collected from the eye socket once a week and blood biochemistry analysis were performed using a fully automatic biochemistry analyzer (ADVIA2400, Siemens, Chicago, USA). Representative inflammatory cytokines were determined by enzyme-linked immunosorbent assay (PBL Biomedical Laboratories and BD Biosciences, Shanghai, China) according to the manufacturer's instructions.

2.14. Statistical analysis

Data are presented as mean ± SD. Statistical significance was calculated with a Student's t-test for two groups or one-way ANOVA for multiple groups, followed by a post hoc Tukey's test. Statistical significances are indicated as: *P < 0.05, **P < 0.01, and ***P < 0.001.

The other detailed experimental methods (including sectional *in vitro* study and *in vivo* animal experiments) can be found in the Supplementary Material.

3. Results and discussion

3.1. Design, construction and characterization of G/A@$CaCO_3$-PEG nanocatalyst

AQDs and GOD were co-encapsulated in $CaCO_3$ by employing a gentle co-precipitation method (Scheme 1). The main method to obtain 2D materials with single-layer morphology is mechanical exfoliation method. However, it is currently limited by the low yield [41]. Epitaxial growth methods typically refer to a crystalline layer is deposited on a crystalline substrate by depositing antimony atoms, which has been employed for the preparation of few-layer antimonene. But this method is still subject to various limitations including the high cost and complexity [42]. As a large-scale exfoliation strategy, liquid phase exfoliation has been successfully applied to for mass production of single or few layers of antimonene [31]. In this work, uniform AQDs were initially synthesized by a liquid phase exfoliation approach [34]. In order to enable better physiological dispersity and stability, the AQDs were further functionalized with 1,2-distearoyl-*sn*-glycero-3-phosphoethanolamine poly (ethylene glycol) (DSPE-PEG) via both hydrophobic interactions and van der Waals forces [43]. As expected, these PEGylated AQDs exhibit better dispersity in phosphate-buffered saline (PBS) and cell culture medium as compared to the bare AQDs (Fig. S1). TEM image indicates that the PEGylated AQDs feature high dispersity with an average diameter of 6.7 nm (Fig. 1a). The chemical composition of 2D AQDs was analyzed by XPS analysis. Survey XPS spectrum (Fig. 1b) and narrow scan XPS spectra (Figs. 1c and S2) confirm the O and Sb elemental composition of AQDs. Moreover, Raman spectra of the prepared PEGylated AQDs (Fig. S3) show a A_{1g} peak at ≈145 cm^{-1} (out-of-plane vibrational mode) and E_g peak at ≈107 cm^{-1} (in-plane vibrational mode), which is similar to the bulk antimony power [32]. The XRD patterns of the PEGylated AQDs and AQDs were in accordance with the hexagonal phase of antimonene (JCPDS 35–0732, Fig. S4) [34]. Also, the PEGylated AQDs display broad and dose-dependent absorption ranging from the UV to NIR region (Fig. S5), which potentiates their PA imaging and PTT capabilities.

To protect the AQDs and deliver them into tumor cells, the tumor microenvironment-sensitive $CaCO_3$ NPs were used as a nanocarrier. The co-encapsulation of AQDs and GOD was conducted through a co-precipitation process. Typically, GOD and AQDs were added into an ethanol solution containing Ca^{2+} ions before any precipitate appeared, to ensure that GOD and AQDs were encapsulated effectively. Then, CO_2 and NH_3 gas generated by the thermal decomposition of NH_4HCO_3 would continuously diffuse into the ethanol solution, continually providing the carbonate ions and an alkaline environment to triggers the formation of G/A@$CaCO_3$ NPs. The obtained G/A@$CaCO_3$ NPs were coated with lipid bilayers composed of 1,2-dioleoyl-*sn*-glycero-3-phosphate (DOPA), cholesterol, and 1,2-dihexadecanoyl-*sn*-glycero-3-phosphocholine (DPPC) and were further modified with DSPE-PEG to improve physiological stability (Fig. S6) [38,44]. The bare $CaCO_3$ NPs show uniform spherical shapes with an average diameter of 108 nm, as visualized under TEM (Fig. 1d). For G/A@$CaCO_3$-PEG NPs, the encapsulated payloads had no obvious influence on the diameter and morphology of the initial $CaCO_3$ structures (Fig. 1e). The G/A@$CaCO_3$-PEG NPs could be well dispersed in water, phosphate buffer saline

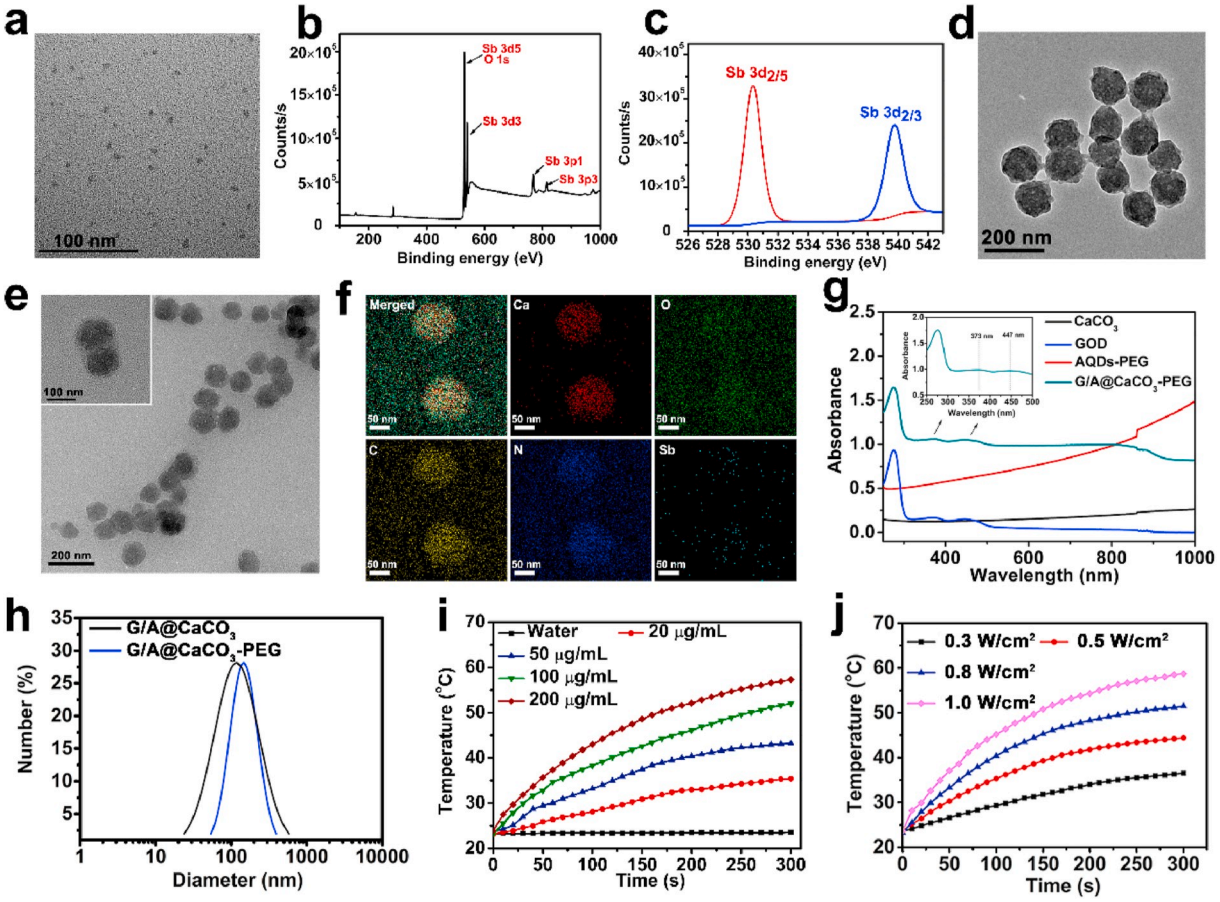

Fig. 1. (a) TEM image and (b) XPS spectrum of the PEGylated AQDs. (c) Narrow scan XPS spectra of PEGylated AQDs for Sb 3d. (d) TEM image of $CaCO_3$ NPs. (e) TEM (magnified image as inset) and (f) elemental-mapping images of G/A@$CaCO_3$-PEG. (g) UV–vis absorption spectra of $CaCO_3$, GOD, AQDs-PEG and G/A@$CaCO_3$-PEG. (h) Particle-size distribution of G/A@$CaCO_3$ and G/A@$CaCO_3$-PEG. (i) Photothermal heating curves of water and G/A@$CaCO_3$-PEG at different concentrations under 808 nm laser irradiation (0.8 W/cm^2) for 5 min. (j) Photothermal heating curves of G/A@$CaCO_3$-PEG (100 μg/mL) under varied power densities laser irradiation for 5 min.

(PBS), and cell-culture medium, without detectable aggregation (Fig. S7). Elemental mapping using high-angle annular dark field scanning TEM (HAADF-STEM) analysis (Fig. 1f) clearly validates the uniform distribution of C, O, Ca, Sb, and N (present in GOD) throughout the G/A@$CaCO_3$-PEG NPs. As shown in electron energy loss spectroscopy (EELS) spectrum (Fig. S8), a noticeable N–K edge is detected in the EELS spectrum of G/A@$CaCO_3$-PEG, while is not present in A@$CaCO_3$-PEG, indicating the successful encapsulation of GOD. Furthermore, the characteristic absorption peaks of GOD at 373 and 447 nm were observed in the UV–Vis absorption spectrum of G/A@$CaCO_3$-PEG (Fig. 1g). The loading of GOD and Sb was calculated to be 16.8% ± 1.9% and 12.7% ± 2.6% (w/w) by using the Bradford protein assay and inductively coupled plasma optical emission spectrometer (ICP-OES), respectively. The hydrodynamic diameters of G/A@$CaCO_3$-PEG and G/A@$CaCO_3$ were 126 ± 6.3 and 114 ± 4.8 nm, respectively, as indicated by DLS data (Fig. 1h). These results collectively signified the successful construction of G/A@$CaCO_3$-PEG nanocatalyst. Meanwhile, the AQD-loaded $CaCO_3$-PEG (A@$CaCO_3$-PEG) NPs with an average diameter of ≈104 nm (Fig. S9) was prepared by following the same procedure except the adding of GOD.

Due to the presence of AQDs, the resulting G/A@$CaCO_3$-PEG features strong NIR absorption (Fig. 1g). Then, the performance of G/A@$CaCO_3$-PEG on photothermal conversion was examined. As a result, both PEGylated AQDs and G/A@$CaCO_3$-PEG NPs exhibited an obvious temperature elevation after exposure to NIR irradiation (Fig. S10). From the temperature vs time profiles (Fig. 1i and j) and photothermal images (Fig. S11), a concentration- and laser power density-dependent temperature elevation was observed. The temperature of a 100 μg/mL G/A@$CaCO_3$-PEG solution changed from 23.7 to 45.2 °C after 808 nm laser (0.5 W/cm^2) irradiation for 5 min. The photothermal-conversion efficiency (η) of G/A@$CaCO_3$-PEG was calculated to be as high as 42.4% (Fig. S12). The η values of other previously reported photothermal agents were summarized in Table S1. Clearly, the η of G/A@$CaCO_3$-PEG is higher than some other previously reported 2D antimonenes-based nanomaterials and typical photothermal nanoagents such as Au nanorods (21%) [45], $Cu_{2x}Se$ nanocrystals (22%) [46], black phosphorus quantum dots (28.4%) [47], and comparable to Sb nanorod bundles (41%) [48]. Despite the encapsulation of $CaCO_3$ lowered the photothermal-conversion efficiency to some extent (from 45.5% to 42.4%), such a high η value is still sufficiently high to achieve desirable low-temperature PTT. In cyclic photothermal evaluation, the high photothermal stability was observed, with largely constant temperature changes during five heating/cooling cycles (Fig. S13).

The decomposition profiles of the G/A@$CaCO_3$-PEG NPs were then assessed in PBS at pH 5.0, 6.5 and 7.4. From the TEM images, G/A@$CaCO_3$-PEG in PBS reveals no significant degradation at pH 7.4 during a 2 h incubation period (Fig. 2a). After co-incubation with PBS at pH 6.5, the time-dependent degradation was observed. The decomposition rate was substantially accelerated at pH 5.0, and no intact $CaCO_3$ structures could be observed after 30 min. The hydrodynamic diameter of G/A@$CaCO_3$-PEG exhibits a downward trend with dispersion time, which is accelerated under reduced pH conditions (Fig. 2b). 37.1% ± 1.8% and 43.6% ± 1.6% of the Ca^{2+} content of the nanocatalysts were released after being incubated at pH 6.5 and 5.0 for 12 h, respectively, whereas only 13.9% ± 3.3% was freed at pH 7.4 (Fig. 2c). Collectively, these results solidly demonstrated the biodegradability of the constructed G/A@$CaCO_3$-PEG nanocatalyst under mildly acidic conditions.

GOD is an endogenous oxido-reductase, which has been used as an "amplifier" for multimodal cancer treatments [39]. To identify that GOD encapsulated in the interior of $CaCO_3$ particles could effectively catalyze the oxidization of glucose into H_2O_2 and gluconic acid, as required for such amplification, glucose decomposition was subsequently evaluated (Fig. 2d). The concentration of glucose decreased rapidly in the presence of G/A@$CaCO_3$-PEG at pH 5.0, which also reflected a concentration-dependent catalytic performance. It is noted that free GOD induced more effective glucose consumption under the same conditions, but the difference is relatively not obvious.

The pH of the glucose solution in the presence of free GOD rapidly

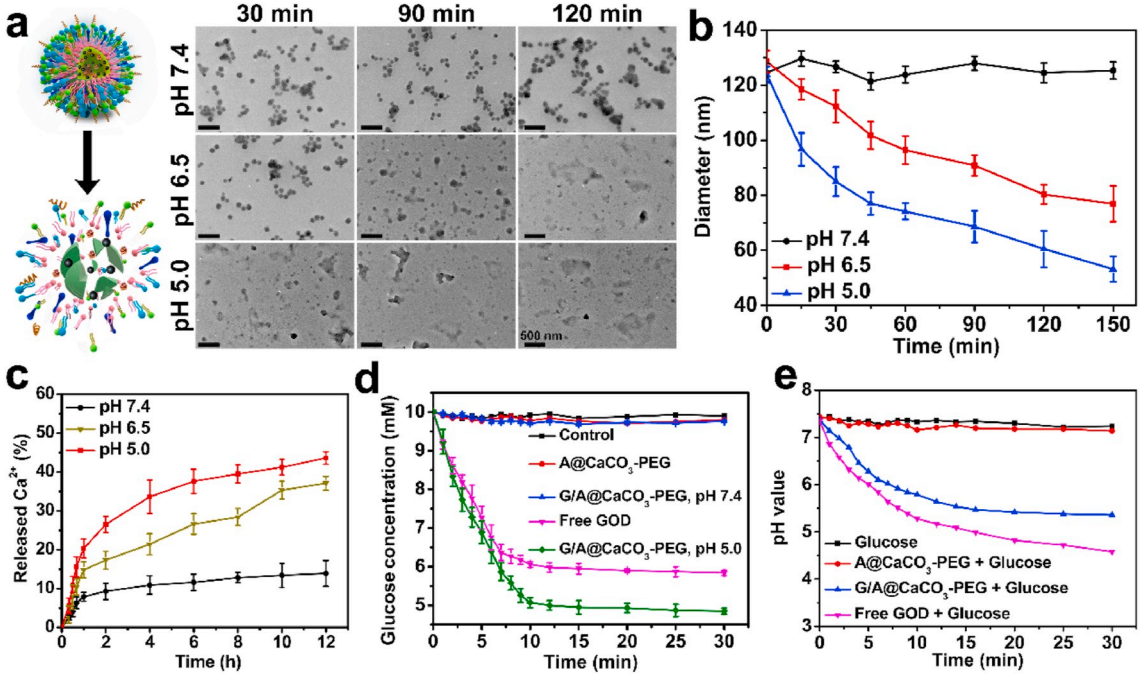

Fig. 2. (a) TEM images of G/A@$CaCO_3$-PEG after incubation in PBS (37 °C) at different pH values (5.0, 6.5 and 7.4) for 2 h. Inset: Schematic illustration showing the pH-responsive decomposition of G/A@$CaCO_3$-PEG NPs. (b) Time-dependent size changes of G/A@$CaCO_3$-PEG in PBS at different pH values, as measured by DLS. Error bars indicate standard deviation (n = 5). (c) Time-dependent Ca^{2+} release from G/A@$CaCO_3$-PEG dispersed in buffer solutions at different pH values. Error bars indicate standard deviation (n = 5). (d) Glucose concentration vs time for different nanoparticle dispersions with the addition of glucose (1.0 mg/mL) and H_2O_2 (50 μM). Error bars indicate standard deviation (n = 3). (e) The change in pH of the glucose solution (1.0 mg/mL) with the addition of A@$CaCO_3$-PEG, G/A@$CaCO_3$-PEG and free GOD.

decreased from 7.3 to 4.6, and then remained at a low level (Fig. 2e), thus confirming that gluconic acid was produced from glucose oxidation. In the presence of G/A@$CaCO_3$-PEG, the pH of the glucose solution decreased from 7.4 to 6.1 in the initial 6 min, and then decreased more slowly to 5.4 after reaction for 30 min, indicating that G/A@$CaCO_3$-PEG could decompose glucose into gluconic acid, and H^+ thereby generated could be further exploited for accelerating $CaCO_3$ dissolution. Moreover, the stability of the enzymatic activity after $CaCO_3$ encapsulation was evaluated by monitoring the UV–vis absorption of catalysate. As shown in Fig. S14, G/A@$CaCO_3$-PEG exhibited a comparable catalytic activity by equivalent free GOD, demonstrating the inconspicuous conversion of enzymatic activity after encapsulated into $CaCO_3$. These results elucidated that the engineered G/A@$CaCO_3$-PEG nanocatalyst retained sufficient GOD bioactivity to catalyze the oxidation of glucose, which laid the foundation for subsequent effectively blocking the energy supply of ATP and starving the tumor cells.

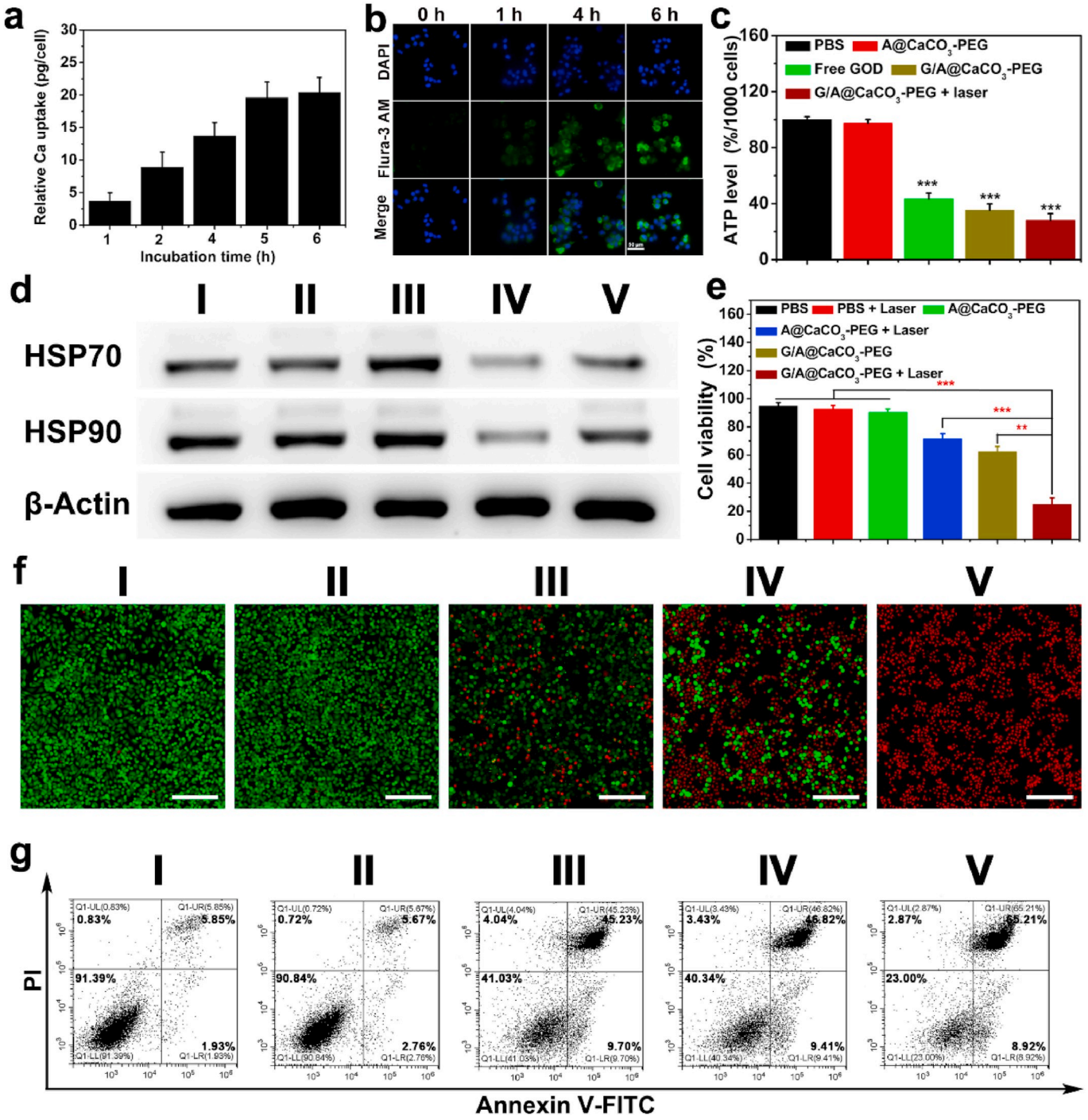

Fig. 3. (a) The uptake of Ca by SW1990 cells at different times (0, 1, 2, 4, 5, and 6 h) after treatment with G/A@$CaCO_3$-PEG NPs (n = 5). (b) Confocal images of SW1990 cells incubated with G/A@$CaCO_3$-PEG NPs (Ca^{2+}: 4 mM) and stained with an intracellular Ca^{2+} indicator (Flura-3 AM). Scale bar: 50 μm. (c) ATP levels in SW1990 cells after different treatments (n = 6, ***P < 0.001). (d) Western blotting analysis of HSP70 and HSP90 expression in SW1990 cells. (e) Relative viabilities of SW1990 cells after different treatments, quantified by CCK-8 assay (n = 6). **P < 0.01, ***P < 0.001. (f) Confocal images of SW1990 cells stained with calcein-AM and PI after various treatments. (g) Flow cytometry analysis of annexin V-FITC/PI-stained SW1990 cells. In panels d, f, g treatment groups are denoted as: (I) untreated cells control, (II) A@$CaCO_3$-PEG, (III) A@$CaCO_3$-PEG + laser, (IV) G/A@$CaCO_3$-PEG, and (V) G/A@$CaCO_3$-PEG + laser.

3.2. In vitro cellular uptake and intracellular ATP quantification

Before evaluating the feasibility of G/A@$CaCO_3$-PEG for synergistic therapy, cellular uptake and ATP inhibition efficacy were initially assessed. The cytotoxicity of $CaCO_3$-PEG was examined on murine fibroblast cell line (L929), murine breast cancer cell line (4T1), human pancreatic carcinoma cell line (SW1990) and human prostate cancer cell line (PC3 cell) via a cell counting kit-8 (CCK-8) assay. No obvious cytotoxicity can be observed in these cell lines even at the co-incubation concentration of as high as 200 μg/mL (Fig. S15), indicating the high cytocompatibility. Also, the cytotoxicity of G/A@$CaCO_3$-PEG was assessed in various normal somatic cells (L929 and HUVEC). After treated with different concentrations of G/A@$CaCO_3$-PEG, there is no obvious differences on cytotoxicity detected in both L929 and HUVEC cells (Fig. S16), indicating the low cytotoxicity of G/A@$CaCO_3$-PEG to normal somatic cells, even at the concentration of as high as 250 μg/mL for 24 h. Cellular uptake was evaluated by measuring total Ca and Sb levels within G/A@$CaCO_3$-PEG-treated SW1990 cells by using ICP-OES. Fig. 3a shows that the cellular internalization of G/A@$CaCO_3$-PEG increased with time, and the cellular Ca content reached about 20.4 pg/cell after 6 h of incubation. Qualitative analysis of the cellular Sb uptake presented mirror results, with the highest Sb level (10.6 pg/cell) detected after 6 h co-incubation (Fig. S17). The intracellular uptake of G/A@$CaCO_3$-PEG was monitored with the Flura-3 AM Ca^{2+} probe (Fig. 3b), which confirmed the uptake pattern. These results suggested that G/A@$CaCO_3$-PEG could be efficiently uptaken by cells, allowing intracellular GOD release and subsequent ATP inhibition.

To investigate ATP inhibition, we initially explored how it was affected by GOD concentration. A clear concentration-dependent decline in ATP levels was detected with the elevated GOD concentration (Fig. S18). The ATP level in SW1990 cells was then quantified after a range of different treatments. As shown in Fig. 3c, the ATP level in the GOD (43.3%) and G/A@$CaCO_3$-PEG (35.3%) group has been significantly reduced compared to the PBS group, and the ATP level in the G/A@$CaCO_3$-PEG + NIR group was even lower (28.1%). In addition, A@$CaCO_3$-PEG treatment did not result in obvious ATP inhibition, which confirmed the GOD-induced restriction of ATP supply.

3.3. Down-regulation of HSP expression at cellular level

It has been demonstrated that tumor thermoresistance is dominantly caused by HSPs, a pathway which relies on energy supply from ATP [49,50]. Thus, retarding ATP generation is expected to surmount the tumor thermoresistance. The expression of HSPs (HSP70 and HSP90) in SW1990 cells receiving different treatments was evaluated by Western blot analysis. As expected, high HSP70 and HSP90 expression levels were detected in the cells treated with A@$CaCO_3$-PEG after NIR laser irradiation (Fig. 3d), presumably because of the defensive heat shock response. Both GOD and G/A@$CaCO_3$-PEG treatments significantly retarded the HSP70 and HSP90 expression levels, validating that interfering ATP generation can inhibit the overexpression of HSP. Quantifying the level of HSPs in SW1990 cells post various treatments (Fig. S19) reveals that HSP70 levels increased by 1.44-fold after the A@$CaCO_3$-PEG + NIR treatment, while that of HSP90 was 1.12-fold greater. In comparison, the relative HSP70 and HSP90 levels were reduced dramatically to 1.93 and 2.38-fold with G/A@$CaCO_3$-PEG. Furthermore, a similar trend has also been achieved for the expression of other HSP proteins (HSP60 and HSP110) after different treatments (Fig. S20), indicating the generality of GOD-induced restricted ATP strategy for consequent HSP inhibition. Collectively, these results demonstrate that G/A@$CaCO_3$-PEG could be an effective adjuvant to augment Sb-based PTT by down-regulating HSPs expression.

3.4. In vitro low-temperature PTT

The strategy behind the G/A@$CaCO_3$-PEG nanoplatform depends on the use of GOD to inhibit HSP expression through reducing ATP production, thereby augmenting the low-temperature PTT efficacy of the AQDs. The *in vitro* anticancer efficacy of G/A@$CaCO_3$-PEG was assessed on SW1990 cancer cells. As expected, the cell viabilities were dependent on the dose of G/A@$CaCO_3$-PEG and the laser power density (Fig. S21). Based on these results, an NIR laser at 0.8 W/cm^2 was utilized to trigger low-temperature PTT. The relative viabilities of the cells after treatment with A@$CaCO_3$-PEG + laser and G/A@$CaCO_3$-PEG were 71.4 ± 3.8% and 62.4 ± 3.7%, respectively (Fig. 3e). These relatively high values arise as result of the relatively small effect of low-temperature PTT or GOD induced-glucose depletion alone. This unsatisfactory therapeutic effect revealed that the monotherapy was ineffective. After treatment with G/A@$CaCO_3$-PEG upon laser irradiation, cell viability decreased substantially to 24.8 ± 4.7%. Calcein AM/PI double staining assays also confirmed higher apparent cell death after treatment with G/A@$CaCO_3$-PEG + laser than with the other treatments (Fig. 3f). In addition, we also investigated the apoptotic signaling pathway by Western blot assay (Fig. S22). It can be observed that the cell after treatment with G/A@$CaCO_3$-PEG under laser irradiation induces maximal Bcl-2 down-regulation and synchronously displays the largest up-regulations of both Bax and Caspase-3 protein expressions, which indicates the activation of low-temperature PTT-mediated apoptosis pathway. These findings were further verified by quantitative flow cytometry analysis (Fig. 3g). G/A@$CaCO_3$-PEG in the absence of laser irradiation induced moderate cell apoptosis (61.3%) due to the starvation effect of GOD. The G/A@$CaCO_3$-PEG + laser treatment was most effective in promoting cell apoptosis/necrosis (70.7%). These results uncovered that the G/A@$CaCO_3$-PEG in combination with laser irradiation would induce apparent cell apoptosis via low-temperature PTT by ATP inhibition-induced HSP down-regulation and GOD-mediated glucose depletion.

3.5. In vivo PA imaging performance, biodistribution, and metabolism

PA imaging has become one of the most promising alternatives to conventional optical imaging, due to its high sensitivity, deep detection, and high spatial resolution [51]. Since G/A@$CaCO_3$-PEG exerted excellent photothermal performance and intense NIR absorption, the potential of G/A@$CaCO_3$-PEG as a PA-imaging contrast agent was assessed both *in vitro* and *in vivo*. A clear Sb concentration-dependent enhancement of PA signals was observed, with the PA values displaying linear correlation with the Sb concentration (Fig. 4a). For PA imaging *in vivo*, SW1990 tumor-bearing mice were intravenously administrated with G/A@$CaCO_3$-PEG followed by PA imaging at different time points. Intuitively, the PA signal intensity from the tumor region strengthens gradually over time (Fig. 4b). The enhanced PA signals at the tumor site were apparent at 12 h post-injection, and sustained for as long as 24 h, as evidenced by the quantitative analysis of each PA signal (Fig. S23). These results indicated potent PA imaging performance and significant tumor accumulation of G/A@$CaCO_3$-PEG.

The blood-circulation profile of G/A@$CaCO_3$-PEG was evaluated using ICP-OES, by measuring the concentrations of Sb in blood taken from the mice at different time points (Fig. S24). The blood levels of G/A@$CaCO_3$-PEG decreased gradually over time in agreement with a two-compartment model with long circulation time ($t_{1/2(\alpha)}$ = 1.98 ± 0.63 h, $t_{1/2(\beta)}$ = 15.72 ± 2.84 h). This prolonged circulation time should be advantageous for effective tumor accumulation of G/A@$CaCO_3$-PEG via the enhanced permeability and retention (EPR) effect, which was further confirmed by the biodistribution experiments (Fig. 4c). Despite the G/A@$CaCO_3$-PEG NPs accumulate in reticuloendothelial system organs, such as the liver (16.4%) and spleen (14.8%), significant tumor accumulation at ≈ 7.6% ID/g was observed 12 h post injection. By recording the Sb contents in feces and urine samples, it was found that both feces and urine exhibit highest Sb amounts at 2 days post-injection and the values then decreased with time (Fig. S25). This phenomenon indicates that G/A@$CaCO_3$-PEG could be effectively and rapidly eliminated from the body. Such tumor accumulation and rapid clearance properties of G/

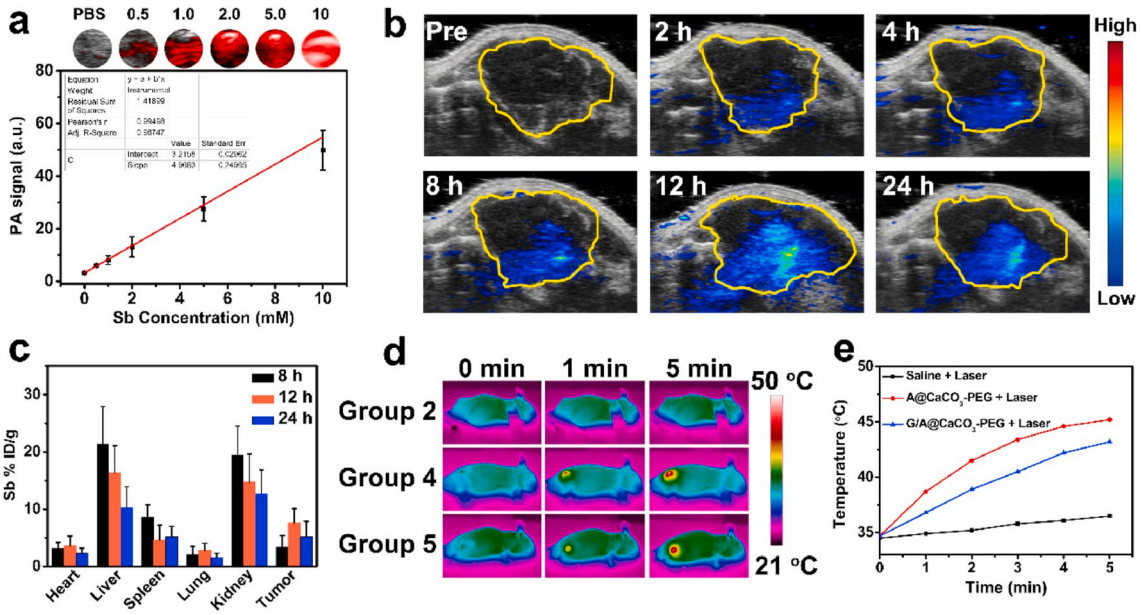

Fig. 4. (a) *In vitro* PA images and signals of G/A@$CaCO_3$-PEG in aqueous suspension at different concentrations of Sb (n = 3). (b) *In vivo* PA images of SW1990 tumor-bearing mice at different time points after intravenous injection of G/A@$CaCO_3$-PEG. The yellow circles indicate the tumor sites. (c) Biodistribution of Sb in the major organs and tumor after intravenous injection of G/A@$CaCO_3$-PEG (n = 3). (d) Infrared thermal images and (e) temperature curves of tumor-bearing mice intravenously injected with saline (group 2), A@$CaCO_3$-PEG (group 4) and G/A@$CaCO_3$-PEG (group 5) and then irradiated with an 808 nm NIR laser (0.8 W/cm^2) for 5 min.

A@$CaCO_3$-PEG should enable effective cancer-combinatorial therapy.

3.6. *In vivo* tumor therapy enabled by engineered G/A@$CaCO_3$-PEG nanocatalyst

To assess and reveal the therapeutic efficacy *in vivo*, SW1990 tumor-bearing mice were randomly divided into five groups (n = 3 in each group): 1) saline (control), 2) saline + laser (laser), 3) G/A@$CaCO_3$-PEG, 4) A@$CaCO_3$-PEG + laser (low-temperature PTT), and 5) G/A@$CaCO_3$-PEG + laser (synergistic therapy). Groups 2, 4 and 5 were irradiated with an NIR laser (0.8 W/cm^2) for 5 min at 12 h post-injection to trigger low-temperature PTT (Fig. 4d). For mice receiving A@$CaCO_3$-PEG and G/A@$CaCO_3$-PEG, 5 min laser irradiation at a low power density resulted in an elevation of tumor temperature to about 43 °C (Fig. 4e), which is within the temperature range for low-temperature PTT. After different treatments, the volume of the tumors was calculated every 2 days (Fig. 5a). Rapid tumor growth was evident in the saline-treated group, and laser irradiation alone displayed a negligible inhibition effect. With regard to the treatment of G/A@$CaCO_3$-PEG alone, tumor growth was also not effectively inhibited (inhibition rate: 38.4%). This was additionally the case for mice treated with A@$CaCO_3$-PEG plus laser irradiation (inhibition rate: 45.5%). These findings are attributed to the low efficacy of GOD-mediated glucose depletion or low-temperature PTT alone.

In comparison, the tumor growth of mice in group 5 (G/A@$CaCO_3$-PEG + laser) was efficiently suppressed (inhibition rate: 83.9%), which is due to the synergistic effect of GOD-mediated starvation therapy and low-temperature PTT. The tumor weights (Fig. 5b) and corresponding photographs (Fig. 5c) clearly substantiate the therapeutic effect of G/A@$CaCO_3$-PEG nanocatalysts with laser irradiation. The most significant large-area cell shrinkage and karyopyknosis in hematoxylin and eosin (H&E) staining and the most distinct cancer-cell apoptosis as observed terminal deoxynucleotidyl transferase dUTP nick end labeling (TUNEL) staining are also observed after the treatment with G/A@$CaCO_3$-PEG combined with NIR laser irradiation (Fig. 5d). No significant body-weight variations were observed during the therapeutic treatment regimens (Fig. S26), confirming that there was no systemic toxicity of G/A@$CaCO_3$-PEG.

To clarify the underlying mechanism of augmented PTT efficacy in the synergistic therapy group, the *in vivo* expression levels of HSP70 (red) and HSP90 (green) were determined by immunofluorescence staining analysis (Fig. 5e). The expression was markedly increased after hyperthermia treatment (A@$CaCO_3$-PEG + laser), while treatment with G/A@$CaCO_3$-PEG led to dramatically down-regulated HSP90 expression, even after laser irradiation. By quantifying the intratumoral ATP levels post various treatments, it was observed that mice treated by G/A@$CaCO_3$-PEG, with or without NIR irradiation, had notably lower ATP levels (Fig. S27). In contrast, tumor ATP levels in the A@$CaCO_3$-PEG + laser treatment group remained at 90.6%, which is similar with the PBS control group. On basis of this proof-of-concept evaluation, it is clearly that the augmentation of PTT was attributed to HSP suppression mediated by GOD-induced restrictions in ATP supply, which could effectively reverse thermoresistance during a hyperthermia treatment.

To guarantee the potential for further clinical translation, the *in vivo* biosafety of G/A@$CaCO_3$-PEG was evaluated by histological examinations of main organs and a hematology assay. The H&E staining results reveals that no obvious organ damage occurred with the different treatments (Fig. S28), reflecting the high histocompatibility of G/A@$CaCO_3$-PEG at the dosage used (Sb: 3.5 mg/kg). For the hematology assay, the blood of healthy Kunming mice intravenously injected with PBS or G/A@$CaCO_3$-PEG was collected at 1, 7 and 14 days post-injection. The G/A@$CaCO_3$-PEG-treated group displayed no significant variation in the measured serum indexes as compared to the PBS control group, and all parameters laid in the normal range (Fig. S29). All these results confirm the high biosafety/biocompatibility of the engineered G/A@$CaCO_3$-PEG nanocatalysts.

4. Conclusions

In summary, a potent pH-sensitive nanocatalyst (G/A@$CaCO_3$-PEG) has been constructed via the rational integration of calcium-based biomineral and single-element 2D nanomaterials. The nanocatalyst was engineered to overcome the tumor thermoresistance for augmenting the therapeutic efficiency of photonic hyperthermia through a "non-

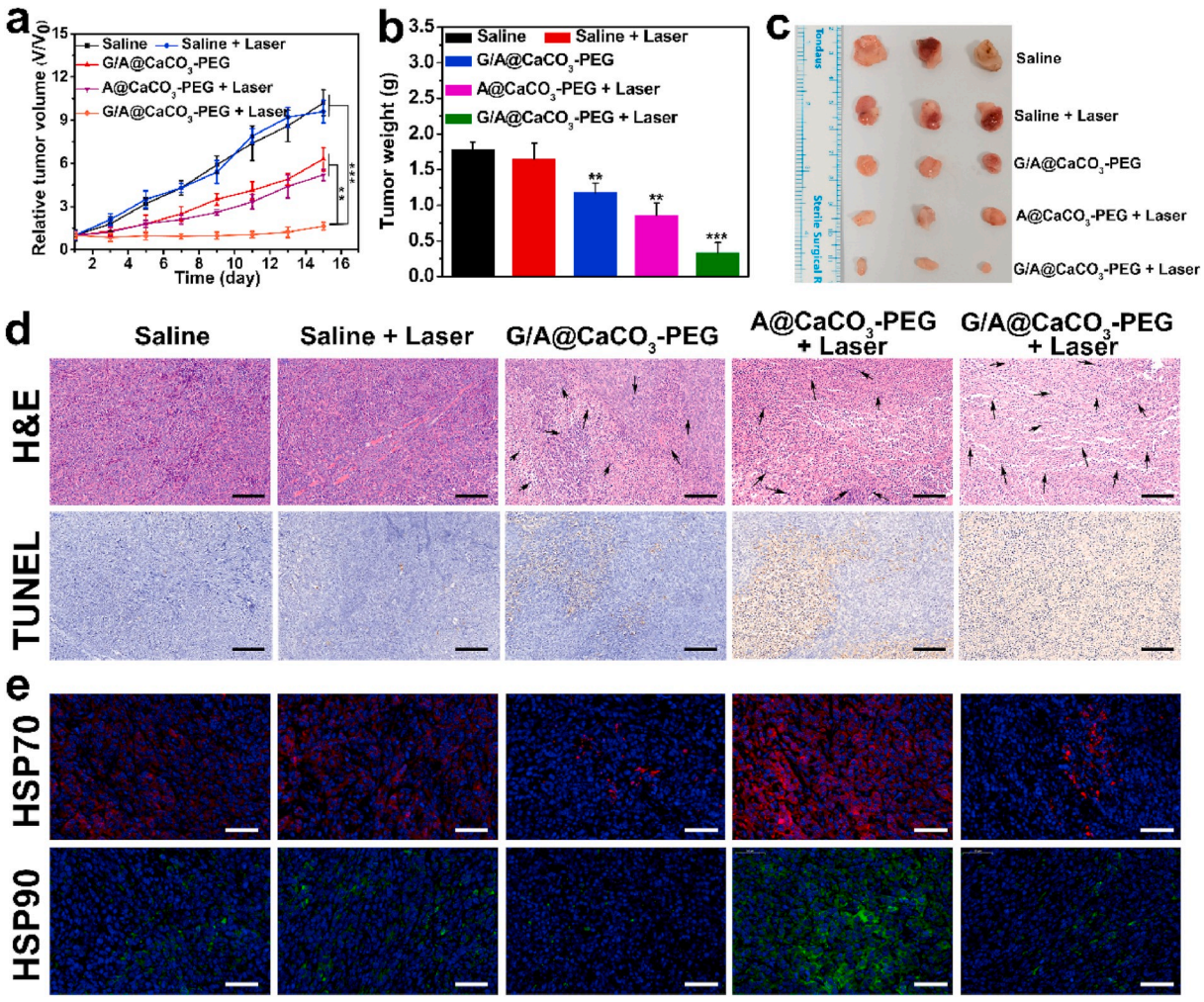

Fig. 5. (a) Tumor-volume changes as a function of time after varied treatments (n = 3). (b) Tumor weights of mice on the 15th day at the end of treatment. **P < 0.01 and ***P < 0.001. (c) Digital photographs of tumors collected on day 15. (d) H&E and TUNEL staining of tumor tissues collected from different treatments. The black arrow represents the site of cell shrinkage and karyopyknosis. (e) The HSP70 and HSP90 expression in tumors collected from mice after various treatments as determined by immunofluorescence staining. Scale bar: 50 μm.

inhibitor involvement" strategy. A composite nanocatalyst was fabricated by incorporating 2D antimonene QDs and glucose oxidase (GOD) into biodegradable $CaCO_3$ NPs. Once internalized into the cancer cells, G/A@$CaCO_3$-PEG underwent rapid decomposition within the mildly acidic tumor microenvironment. Subsequently, the released GOD effectively exhausted endogenous glucose to block the cells' energy supply. The GOD-induced restriction on ATP supply could also downregulate HSP expression, subsequently reversing the thermoresistance of the cancer cells. Extensive and systematic *in vitro* and *in vivo* evaluations solidly confirmed that remarkable antitumor performance was achieved, originating from the glucose depletion and the augmented low-temperature PTT synergistic treatment, without obvious side effects. This engineered nanoplatform also featured intrinsic PA imaging capability, potentiating the therapeutic guidance and monitoring. This work not only broadens the biomedical use of pH-dissociable calcium-based nanomedicines, but also provides an intriguing strategy for reversing the thermoresistance of cancer cells in hyperthermia-related nanotherapies.

CRediT authorship contribution statement

Jianrong Wu: Conceptualization, Investigation, Data curation, Methodology, Formal analysis, Validation, Funding acquisition, Writing – original draft. **Xiaojun Cai:** Investigation, Data curation, Funding acquisition, Methodology, Resources, Software. **Gareth R. Williams:** Writing – review & editing. **Zheying Meng:** Methodology, Formal analysis, Investigation. **Weijuan Zou:** Investigation, Methodology, Software. **Li Yao:** Software, Investigation, Validation. **Bing Hu:** Supervision, Resources. **Yu Chen:** Resources, Supervision, Writing – review & editing, Project administration. **Yuanyi Zheng:** Conceptualization, Funding acquisition, Writing – review & editing, Supervision, Project administration.

Declaration of competing interest

The authors declare no competing financial interest.

Acknowledgements

We greatly acknowledge the financial support from the NSFC Key Projects of International Cooperation and Exchanges (Grant No. 81720108023), National Key R&D Program of China (Grant No. 2018YFC0115200), National Natural Science Foundation of China (Grant No. 82001943), Translational medicine national science and technology infrastructure (Shanghai) open project fund (TMSK-2020-004), and China Postdoctoral Science Foundation (2020M681331, 2021T140458).

Appendix A. Supplementary data

Supplementary data to this article can be found online at https://doi.org/10.1016/j.bioactmat.2021.08.018.

References

[1] M. Durante, R. Orecchia, J.S. Loeffler, Charged-particle therapy in cancer: clinical uses and future perspectives, Nat. Rev. Clin. Oncol. 14 (2017) 483–495.
[2] M.A. Kotterman, D.V. Schaffer, Engineering adeno-associated viruses for clinical gene therapy, Nat. Rev. Genet. 15 (2014) 445–451.
[3] Z. Xie, T. Fan, J. An, W. Choi, Y. Duo, Y. Ge, B. Zhang, G. Nie, N. Xie, T. Zheng, Y. Chen, H. Zhang, J.S. Kim, Emerging combination strategies with phototherapy in cancer nanomedicine, Chem. Soc. Rev. 49 (2020) 8065–8087.
[4] Y. Kenry, Y. Duan, B. Liu, Recent advances of optical imaging in the second near infrared window, Adv. Mater. 30 (2018), 1802394.
[5] E. Cazares-Cortes, S. Cabana, C. Boitard, E. Nehlig, N. Griffete, J. Fresnais, C. Wilhelm, A. Abou-Hassan, C. Menager, Recent insights in magnetic hyperthermia: from the "hot-spot" effect for local delivery to combined magneto-photo-thermia using magneto-plasmonic hybrids, Adv. Drug Deliv. Rev. 138 (2019) 233–246.
[6] C.S. Kumar, F. Mohammad, Magnetic nanomaterials for hyperthermia-based therapy and controlled drug delivery, Adv. Drug Deliv. Rev. 63 (2011) 789–808.
[7] H. Kim, S. Beack, S. Han, M. Shin, T. Lee, Y. Park, K.S. Kim, A.K. Yetisen, S.H. Yun, W. Kwon, S.K. Hahn, Multifunctional photonic nanomaterials for diagnostic, therapeutic, and theranostic applications, Adv. Mater. 30 (2018), 1701460.
[8] Y. Lu, A.A. Aimetti, R. Langer, Z. Gu, Bioresponsive materials, Nat. Rev. Mater 1 (2016) 16075.
[9] Z. Xie, T. Fan, J. An, W. Choi, Y. Duo, Y. Ge, B. Zhang, G. Nie, N. Xie, T. Zheng, Y. Chen, H. Zhang, J.S. Kim, Emerging combination strategies with phototherapy in cancer nanomedicine, Chem. Soc. Rev. 49 (2020) 8065–8087.
[10] G. Gao, Y.W. Jiang, Y. Guo, H.R. Jia, X. Cheng, Y. Deng, X.W. Yu, Y.X. Zhu, H. Y. Guo, W. Sun, X. Liu, J. Zhao, S. Yang, Z.W. Yu, F.M. S Raya, G. Liang, F.G. Wu, Enzyme-mediated tumor starvation and phototherapy enhance mild-temperature photothermal therapy, Adv. Funct. Mater. 30 (2020), 1909391.
[11] H. Luo, Q. Wang, Y. Deng, T. Yang, H. Ke, H. Yang, H. He, Z. Guo, D. Yu, H. Wu, H. Chen, Mutually synergistic nanoparticles for effective thermo-molecularly targeted therapy, Adv. Funct. Mater. 27 (2017), 1702834.
[12] K.F. Chu, D.E. Dupuy, Thermal ablation of tumours: biological mechanisms and advances in therapy, Nat. Rev. Canc. 14 (2014) 199–208.
[13] J.J. Hu, M.D. Liu, F. Gao, Y. Chen, S.Y. Peng, Z.H. Li, H. Cheng, X.Z. Zhang, Photo-controlled liquid metal nanoparticle-enzyme for starvation/photothermal therapy of tumor by win-win cooperation, Biomaterials 217 (2019), 119303.
[14] Y. Guo, H.R. Jia, X. Zhang, X. Zhang, Q. Sun, S.Z. Wang, J. Zhao, F.G. Wu, A glucose/oxygen-exhausting nanoreactor for starvation- and hypoxia-activated sustainable and cascade chemo-chemodynamic therapy, Small 16 (2020), 2000897.
[15] T.M. Badri, K.L. Chen, M.A. Alsiddig, L. Li, Y. Cai, G.L. Wang, Genetic polymorphism in Hsp90AA1 gene is associated with the thermotolerance in Chinese Holstein cows, Cell Stress Chaperones 23 (2018) 639–651.
[16] C. Kumsta, J.T. Chang, J. Schmalz, M. Hansen, Hormetic heat stress and HSF-1 induce autophagy to improve survival and proteostasis in C. elegans, Nat. Commun. 8 (2017) 14337.
[17] Y. Yang, W. Zhu, Z. Dong, Y. Chao, L. Xu, M. Chen, Z. Liu, 1D coordination polymer nanofibers for low-temperature photothermal therapy, Adv. Mater. 29 (2017), 1703588.
[18] K. Zhang, X. Meng, Y. Cao, Z. Yang, H. Dong, Y. Zhang, H. Lu, Z. Shi, X. Zhang, Metal-organic framework nanoshuttle for synergistic photodynamic and low-temperature photothermal therapy, Adv. Funct. Mater. 28 (2018), 1804634.
[19] Y.W. Won, S.-M. Yoon, C.H. Sonn, K.M. Lee, Y.H. Kim, Nano self-assembly of recombinant human gelatin conjugated with R-tocopheryl succinate for Hsp90 inhibitor, 17-AAG, delivery, ACS Nano 5 (2011) 3839–3848.
[20] J. Wu, D.H. Bremner, S. Niu, M. Shi, H. Wang, R. Tang, L. Zhu, Chemodrug-gated biodegradable hollow mesoporous organosilica nanotheranostics for multimodal imaging-guided low-temperature photothermal therapy/chemotherapy of cancer, ACS Appl. Mater. Interfaces 10 (2018) 42115–42126.
[21] O. Genest, S. Wickner, S.M. Doyle, Hsp90 and Hsp 70 chaperones: collaborators in protein remodeling, J. Biol. Chem. 294 (2019) 2109–2120.
[22] M. Haslbeck, S. Weinkauf, J. Buchner, Small heat shock proteins: simplicity meets complexity, J. Biol. Chem. 294 (2019) 2121–2132.
[23] W. Tao, X. Ji, X. Zhu, L. Li, J. Wang, Y. Zhang, P.E. Saw, W. Li, N. Kong, M.A. Islam, T. Gan, X. Zeng, H. Zhang, M. Mahmoudi, G.J. Tearney, O.C. Farokhzad, Two-dimensional antimonene-based photonic nanomedicine for cancer theranostics, Adv. Mater. 30 (2018), 1802061.
[24] D.K. Ji, C. Ménard-Moyon, A. Bianco, Physically-triggered nanosystems based on two-dimensional materials for cancer theranostics, Adv. Drug Deliv. Rev. 138 (2019) 211–232.
[25] B. Yang, Y. Chen, J. Shi, Material chemistry of two-dimensional inorganic nanosheets in cancer theranostics, Chem. 4 (2018) 1284–1313.
[26] Z. Xie, M. Peng, R. Lu, X. Meng, W. Liang, Z. Li, M. Qiu, B. Zhang, G. Nie, N. Xie, H. Zhang, P.N. Prasad, Black phosphorus-based photothermal therapy with aCD47-mediated immune checkpoint blockade for enhanced cancer immunotherapy, Light, Sci. Appl. 9 (2020) 161.
[27] Z. Tang, N. Kong, J. Ouyang, C. Feng, N.Y. Kim, X. Ji, C. Wang, O.C. Farokhzad, H. Zhang, W. Tao, Phosphorus science-oriented design and synthesis of multifunctional nanomaterials for biomedical applications, Matter 2 (2020) 297–322.
[28] M. Luo, T. Fan, Y. Zhou, H. Zhang, L. Mei, 2D black phosphorus-based biomedical applications, Adv. Funct. Mater. 29 (2019), 1808306.
[29] M. Qiu, A. Singh, D. Wang, J. Qu, M. Swihart, H. Zhang, P.N. Prasad, Biocompatible and biodegradable inorganic nanostructures for nanomedicine: silicon and black phosphorus, Nano Today 25 (2019) 135–155.
[30] S. Zhang, S. Guo, Z. Chen, Y. Wang, H. Gao, J. Gómez-Herrero, P. Ares, F. Zamora, Z. Zhu, H. Zeng, Recent progress in 2D group-VA semiconductors: from theory to experiment, Chem. Soc. Rev. 47 (2018) 982–1021.
[31] X. Wang, J. Song, J. Qu, Antimonene: from experimental preparation to practical application, Angew. Chem. Int. Ed. 58 (2019) 1574–1584.
[32] L. Lu, X. Tang, R. Cao, L. Wu, Z. Li, G. Jing, B. Dong, S. Lu, Y. Li, Y. Xiang, J. Li, D. Fan, H. Zhang, Broadband nonlinear optical response in few-layer antimonene and antimonene quantum dots: a promising optical kerr media with enhanced stability, Adv. Opt. Mater. 5 (2017), 1700301.
[33] Y. Chen, M. Wang, K. Zheng, Y. Ren, H. Xu, Z. Yu, F. Zhou, C. Liu, J. Qu, J. Song, Antimony nanopolyhedrons with tunable localized surface plasmon resonances for highly effective photoacoustic-imaging-guided synergistic photothermal/immunotherapy, Adv. Mater. 33 (2021), 2100039.
[34] W. Tao, X. Ji, X. Xu, M.A. Islam, Z. Li, S. Chen, P.E. Saw, H. Zhang, Z. Bharwani, Z. Guo, J. Shi, O.C. Farokhzad, Antimonene quantum dots: synthesis and application as near-infrared photothermal agents for effective cancer therapy, Angew. Chem. Int. Ed. 56 (2017) 1–6.
[35] Y. Liu, Y. Xiao, M. Yu, Y. Cao, Y. Zhang, T. Zhe, H. Zhang, L. Wang, Antimonene quantum dots as an emerging fluorescent nanoprobe for the pH-mediated dual-channel detection of tetracyclines, Small 16 (2020), 2003429.
[36] J. Kou, Y. Wang, X. Liu, X. Zhang, G. Chen, X. Xu, J. Bao, K. Yang, L. Yuwen, Continuous preparation of antimony nanocrystals with near infrared photothermal property by pulsed laser ablation in liquids, Sci. Rep. 10 (2020) 15095.
[37] C. Qi, J. Lin, L.H. Fu, P. Huang, Calcium-based biomaterials for diagnosis, treatment, and theranostics, Chem. Soc. Rev. 47 (2018) 357–403.
[38] Z. Dong, L. Feng, Y. Hao, M. Chen, M. Gao, Y. Chao, H. Zhao, W. Zhu, J. Liu, C. Liang, Q. Zhang, Z. Liu, Synthesis of Hollow Biomineralized $CaCO_3$-polydopamine nanoparticles for multimodal imaging-guided cancer photodynamic therapy with reduced skin photosensitivity, J. Am. Chem. Soc. 140 (2018) 2165–2178.
[39] L.H. Fu, C. Qi, Y.R. Hu, J. Lin, P. Huang, Glucose oxidase-instructed multimodal synergistic cancer therapy, Adv. Mater. 31 (2019), 1808325.
[40] Z. Dong, L. Feng, Y. Hao, Q. Li, M. Chen, Z. Yang, H. Zhao, Z. Liu, Synthesis of $CaCO_3$-based nanomedicine for enhanced sonodynamic therapy via amplification of tumor oxidative stress, Chem. 6 (2020) 1–17.
[41] P. Ares, F. Aguilar-Galindo, D. Rodriguez-San-Miguel, D.A. Aldave, S. Diaz-Tendero, M. Alcami, F. Martin, J. Gomez-Herrero, F. Zamora, Mechanical isolation of highly stable Antimonene under ambient conditions, Adv. Mater. 28 (2016) 6332–6336.
[42] J. Ji, X. Song, J. Liu, Z. Yan, C. Huo, S. Zhang, M. Su, L. Liao, W. Wang, Z. Ni, Y. Hao, H. Zeng, Two-dimensional antimonene single crystals grown by van der Waals epitaxy, Nat. Commun. 7 (2016) 13352.
[43] J.-P. Wei, X.-L. Chen, X.-Y. Wang, J.-C. Li, S.-G. Shi, G. Liu, N.-F. Zheng, Polyethylene glycol phospholipids encapsulated silicon 2,3-naphthalocyanine dihydroxide nanoparticles (SiNcOH-DSPE-PEG(NH_2) NPs) for single NIR laser induced cancer combination therapy, Chin. Chem. Lett. 28 (2017) 1290–1299.
[44] Z. Dong, L. Feng, W. Zhu, X. Sun, M. Gao, H. Zhao, Y. Chao, Z. Liu, $CaCO_3$ nanoparticles as an ultra-sensitive tumor-pH-responsive nanoplatform enabling real-time drug release monitoring and cancer combination therapy, Biomaterials 110 (2016) 60–70.
[45] J. Zeng, D. Goldfeld, Y. Xia, A plasmon-assisted optofluidic (PAOF) system for measuring the photothermal conversion efficiencies of gold nanostructures and controlling an electrical switch, Angew. Chem. Int. Ed. 52 (2013) 4169–4173.
[46] C.M. Hessel, V.P. Pattani, M. Rasch, M.G. Panthani, B. Koo, J.W. Tunnell, B. A. Korgel, Copper selenide nanocrystals for photothermal therapy, Nano Lett. 11 (2011) 2560–2566.
[47] Z. Sun, H. Xie, S. Tang, X.F. Yu, Z. Guo, J. Shao, H. Zhang, H. Huang, H. Wang, P. K. Chu, Ultrasmall black phosphorus quantum dots: synthesis and use as photothermal agents, Angew. Chem. Int. Ed. 54 (2015) 11526–11530.
[48] W. Li, P. Rong, K. Yang, P. Huang, K. Sun, X. Chen, Semimetal nanomaterials of antimony as highly efficient agent for photoacoustic imaging and photothermal therapy, Biomaterials 45 (2015) 18–26.
[49] J. Zhou, M. Li, Y. Hou, Z. Luo, Q. Chen, H. Cao, R. Huo, C. Xue, L. Sutrisno, L. Hao, Y. Cao, H. Ran, L. Lu, K. Li, K. Cai, Engineering of a nanosized biocatalyst for combined tumor starvation and low-temperature photothermal therapy, ACS Nano 12 (2018) 2858–2872.
[50] H.J. Liu, M. Wang, X. Hu, S. Shi, P. Xu, Enhanced photothermal therapy through the in situ activation of a temperature and redox dual-sensitive nanoreservoir of triptolide, Small 16 (2020), 2003398.
[51] L.V. Wang, S. Hu, Photoacoustic tomography: in vivo imaging from organelles to organs, Science 335 (2012) 1458–1462.